COVER SHEET

Title: Monitoring early-age strain and temperature distributions in full-scale steel-concrete composite beams with distributed fiber optic sensors

Authors: Yi Bao
Matthew Hoehler
Lisa Choe
Matthew A. Klegseth
Genda Chen

ABSTRACT

Concrete is subject to temperature gradients and shrinkage-induced strain during curing. Strain variations in concrete can lead to residual stresses and cracks, in particular when the deformation of concrete is restrained. This in turn can affect the mechanical performance and durability of the structure. In this study, a fully-distributed fiber optic sensor is used to monitor the early-age temperature and strain distributions in a 12.8 m long steel-concrete composite beam based on pulse pre-pump Brillouin optical time domain analysis. Telecommunication-grade, single-mode optical fibers were embedded in the concrete of the specimen that consisted of lightweight aggregate concrete on trapezoidal metal deck acting compositely with a steel I-beam via headed shear studs. Emphases were placed on characterizing the temperature and strain distributions in concrete and understanding the effects of composite action on the evolution of strains in the concrete. Non-uniform strain distributions were successfully measured from the distributed fiber optic sensors in the first two days of curing. The spatial distribution of temperatures along the beam was relatively uniform but varied in amplitude due to the hydration reactions. The strain distributions were non-uniform, which is likely due to concrete cracking as the result of restrained shrinkage of the concrete.

Yi Bao, Department of Civil, Architectural and Environmental Engineering, Missouri University of Science and Technology, 1401 N. Pine Street, Rolla, MO 65409, USA.
Matthew Hoehler, Engineering Laboratory, National Institute of Standards and Technology, Gaithersburg, MD 20899.
Lisa Choe, Engineering Laboratory, National Institute of Standards and Technology, Gaithersburg, MD 20899.
Matthew A. Klegseth, Department of Civil, Architectural and Environmental Engineering, Missouri University of Science and Technology, 1401 N. Pine Street, Rolla, MO 65409, USA.
Genda Chen, Department of Civil, Architectural and Environmental Engineering, Missouri University of Science and Technology, 1401 N. Pine Street, Rolla, MO 65409, USA. Corresponding author: gchen@mst.edu

INTRODUCTION

Concrete is one of the most widely used construction materials in the world [1–3]. With appropriate proportioning of cement, sand, coarse aggregates, and water, a series of hydration reactions take place and concrete may be produced which possesses excellent durability and mechanical properties [4–6]; in particular, under compressive loads. Concrete is noncombustible and corrosion resistant [7–9]. After curing, concrete tends to maintain constant structure temperatures due to its low thermal conductivity and large thermal mass, thus saving energy. Although concrete is weak in tension relative to compression, steel elements such as reinforcing bars can be used as tension reinforcement [10, 11]. Both chemical and mechanical bonds form at the interface between concrete and ribbed steel reinforcing bars to ensure effective force transfer [12, 13]. The comparable coefficients of thermal expansion of concrete and steel are also beneficial to the integrity of steel reinforced concrete structures.

However, the early-age behaviors of concrete [14–17] potentially affect the long-term performance of concrete. During the exothermic hydration reactions in concrete, the temperature of the concrete rises while heat energy is released. If there is a substantial increase of temperature in concrete, the rates of hydration reactions and the mechanical properties of the concrete might be significantly affected. Furthermore, the relatively low thermal conductivity of concrete causes a temperature gradient which eventually induces non-uniform stress distribution within restrained concrete. In additional to the thermal effects, concrete is subjected to autogenous and drying shrinkages [16, 17]. If shrinkage of concrete is restrained, cracks may be caused and significantly reduce the mechanical properties, durability, and fire resistance of the concrete. For unrestrained concrete, cracks may still appear [14] due to the heterogeneous nature of concrete. A concrete member may have different amounts of shrinkage at various locations, producing a stress and strain gradient [14]. Also, concrete is self-restrained by adjacent concrete. The shrinkage may quickly occur at the early age which its mechanical strength is not fully developed yet [15]. Therefore, some researchers [18, 19] emphasized that it is important to investigate the early-age behaviors of concrete and steel-concrete composite structures.

Various methods have been developed and implemented to investigate the temperature changes and shrinkage strains in early-age concrete. Corrugated tube specimen [16, 17] and prism specimen are recommended in the ASTM specifications for measurements of autogenous shrinkage and total shrinkage, respectively. However, since the shrinkage is determined by dividing the total length change by the specimen's gauge length, the measured shrinkage represents the average shrinkage of the specimen. To evaluate the localized shrinkage, a single-mode optical fiber [20–23] was embedded to measure the temperature and strain distributions in ultra-high-performance concrete specimens, based on a pre-pump pulse Brillouin optical time domain analysis (PPP-BOTDA) technology [24, 25]. Shrinkage-induced cracking was identified from the measured strain distributions as sharp peaks [26, 27]. However, thus far, there is a lack of research on early-age behaviors of concrete in composite structures in which the presence of steel may potentially influence the development of shrinkage deformation. Strain and temperature variation in concrete could result in residual stresses and cracks, especially when the deformation of concrete is restrained, and thus could significantly affect the mechanical performance and durability of steel-concrete composite structures.

This paper presents the collaborative study with the National Institute of Standards and Technology (NIST) to characterize the early-age behaviors of concrete, including temperature and strain distributions, using distributed fiber optic sensing approach developed by the authors [14, 15]. As future work, the developed approach will be also used to measure the temperature-dependent composite action between concrete slab and

steel beam and temperature distributions of long-span composite floor beams constructed as part of NIST's research project on composite floor systems [28].

SENSING PRINCIPLE

In an optical fiber, Brillouin scattering results from the interaction of an incipient light wave with an acoustic wave that represents the effect of a characteristic density variation along the fiber [29]. In a PPP-BOTDA system, a forward-propagating (incipient) pulse pre-pump light wave is introduced from one end of optical fiber, and a back-propagating continuous probe wave is beamed into the same fiber from the other end. When the frequency difference between the pump pulse and the probe continuous wave matches the Stokes Brillouin frequency of the optical fiber, Brillouin gain will occur. PPP-BOTDA measures the Brillouin scattering spectra along the length of the optical fiber subjected to the combined effect of strains and temperatures [30]. The Brillouin frequency shift of an optical fiber can be related to the combined effect of the applied strain and temperature with respect to the reference strain and temperature. The Brillouin frequency shift is on the order of 9 GHz to 13 GHz for light waves of 1.3 μm to 1.6 μm wavelengths in a single-mode optical fiber.

The Brillouin frequency is dependent on strain and temperature changes. For relatively small changes of strain and temperature, a linear relation can be used as given in Eq. (1).

$$\Delta \nu_B = C_\varepsilon \Delta\varepsilon + C_T \Delta T \tag{1}$$

where C_ε and C_T denote the strain and temperature coefficients, respectively; $\Delta\varepsilon$ and ΔT denote the strain and temperature changes, respectively. The strain and temperature coefficients were calibrated in the laboratory in controlled strain and temperature conditions.

EXPERIMENTAL PROGRAM

Specimen

This experimental study used the 12.8 m long composite floor beam specimens constructed in the National Fire Research Laboratory (NFRL) [31] at NIST for its research project on composite floor systems subject to fire. The lightweight concrete slab measuring 12.8 m × 1.83 m in plan was cast on top of all fluted galvanized metal decking and supported by the W18×35 steel girder, as depicted in Figures 1(a) and 1(b). Due to the profile of the steel deck, the depth of the concrete deck varied from 84 mm to 160 mm, as illustrated in Figure 1(b). The concrete topping was reinforced using a welded wire mesh (6×6 W1.4/W1.4). The concrete deck and steel beams were connected by 19 mm diameter headed shear studs. The spacing between two adjacent shear studs was 305 mm.

First, the steel deck was placed on top of the steel beams, followed by welding the headed shear studs, as shown in Figure 2(a). The studs were welded all the way through the metal deck to the steel beams. A welded wire mesh was supported by small steel chairs, and it was about 20 mm above the top of the metal deck. After the installation of optical fibers, concrete was placed in the formwork.

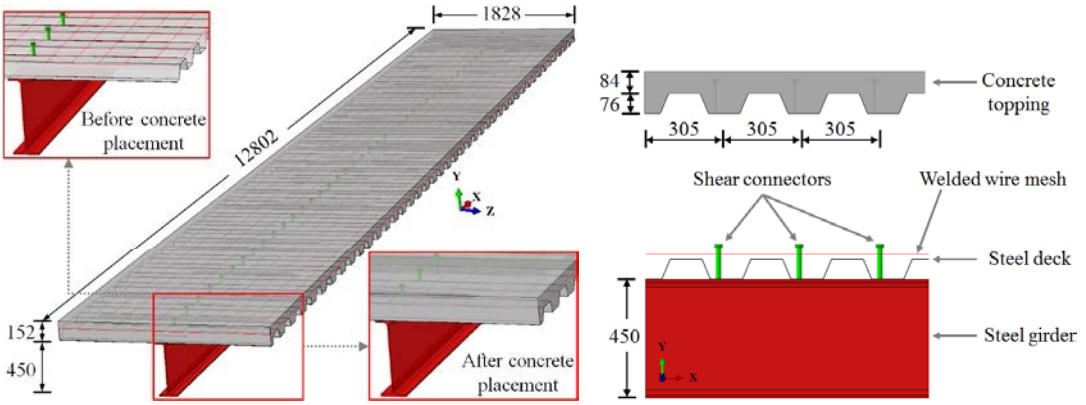

(a) (b)

Figure 1. The steel-concrete composite specimen (unit: mm): (a) three-dimensional illustration; (b) profile of the steel deck.

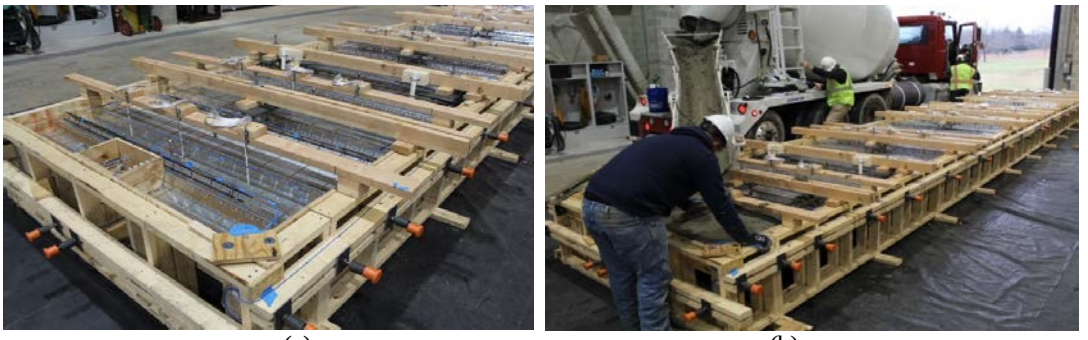

(a) (b)

Figure 2. Photograph of the specimen: (a) before concrete placement; (b) during concrete placement.

Materials Properties

The concrete topping was fabricated using a plastic-fiber reinforced lightweight concrete. The water-to-binder ratio was 0.46. The binder was composed of 25 % Class C fly ash and 75 % Type I Portland cement, by total volume of binder. The Blaine fineness values of the fly ash and cement are 465 m^2/kg and 560 m^2/kg, respectively. Missouri River sand (0 mm to 4.75 mm) with a specific surface area of 2.64 was used at a binder-to-sand ratio of 0.42, by volume. A rotary kiln expanded slate lightweight aggregate (LWA) was used at a sand-to-LWA ratio of 0.88, by volume. Both sand and LWA were pre-treated to ensure the saturated-surface-dry (SSD) condition. A polycarboxylate-based high-range water reducer was used to improve the flowability of the concrete. The dosage of high-range water reducer was adjusted to achieve a slump of 220 mm ± 25 mm. Polypropylene microfibers with a specific gravity of 0.91 were used at a content of 2.37 kg/m^3 of the concrete. The fibers are 40 μm in diameter and 25 mm in length. The tensile strength and Young's modulus of the fibers are 0.35 GPa and 3.45 GPa, respectively.

The concrete was mixed at a commercial batching plant and transported to NIST for placement in ready mix truck. Concrete was placed through the concrete discharging chute of the mixer truck, as depicted in Figure 2(d). After concrete placement, a vibrator was used to consolidate concrete along the formwork carefully to avoid breakage of the optical fibers. The specimen was covered with wet burlap and plastic immediately after specimen casting. The formwork was removed from the specimens after 3 days. The specimen was then cured under wet burlap and plastic sheet at room temperature (22 °C ± 3 °C) until 7 days after casting. Water was sprayed on the burlap to maintain the moisture during the first week of curing. The concrete's density was 2,070 kg/m^3 at 28 days. The compressive strength was 38 MPa at 28 days and 41 MPa at 56 days in accordance with ASTM

C39/C39M. A sensor was used to measure the internal relative humidity of concrete at a depth of 90 mm. In the first 2 days after setting, the internal relatively humidity of the concrete mixture was measured to be 99%–100%. Mechanical properties of the types of steel were provided by the manufacturers. Hot rolled ASTM A992 steel, which is a low carbon structural steel alloy, was used for the steel beams [32]. Its tensile yield strength is 345 MPa; its Young's modulus of elasticity is 200 GPa. Cold drawn steel in compliance with ASTM A108 was used for shear studs. Its tensile yield strength is 414 MPa; its Young's modulus of elasticity is 205 GPa. Grade 65 welded wire steel in compliance with ASTM A185 was used for smooth welded wire fabrics. Its tensile yield strength is 448 MPa; its Young's modulus of elasticity is 200 GPa. Cold rolled ASTM A611 Grade D steel was used for the steel decks. Its tensile yield strength is 276 MPa; its Young's modulus of elasticity is 203 GPa. The density of all the three types of steel is about 7850 kg/m^3.

Instrumentation

A Neubrescope data acquisition system (model: NBX-7020) was used to perform PPP-BOTDA measurements for the distributed fiber optic sensors. A 2 cm spatial resolution was obtainable, with use of a pulse bandwidth of 0.2 ns. The sampling and spatial resolutions in this study were respectively set at 1 cm and 2 cm, meaning that data points were sampled at every 1 cm and the Brillouin frequency shifts of two points spaced at no less than 2 cm could be distinguished. A single-mode optical fiber with polymer coatings was used as a distributed fiber optic sensor for the temperature and strain distributions measurement. The single-mode fiber had an 8.2 μm glass core, a 125 μm glass cladding, a soft inner polymer coating (outer diameter: 190 μm), and a stiff outer polymer coating (outer diameter: 242 μm). The soft and stiff layers provide mechanical protection, and prevent abrasion and environmental exposure for the glass. The distributed fiber optic sensors measure Brillouin frequency shifts due to temperature and/or strain changes. Once calibrated, the sensors can be used to evaluate the temperature and strain changes from the measured Brillouin frequency shifts.

The distributed sensor was embedded in the concrete topping and along the length of the steel girder, as shown in Figures 3(a) and 3(b). The distributed sensor was continuously passed through the points B and A in the concrete topping back and forth to form a loop. The 1st and 2nd paths were at the same location. The distributed sensor in the 1st path was packaged and could slide in a polymer hose with negligible friction, and thus the measurement results are used for temperature compensation for the distributed sensor in the 2nd path. None of the optical fibers was damaged during concrete placement.

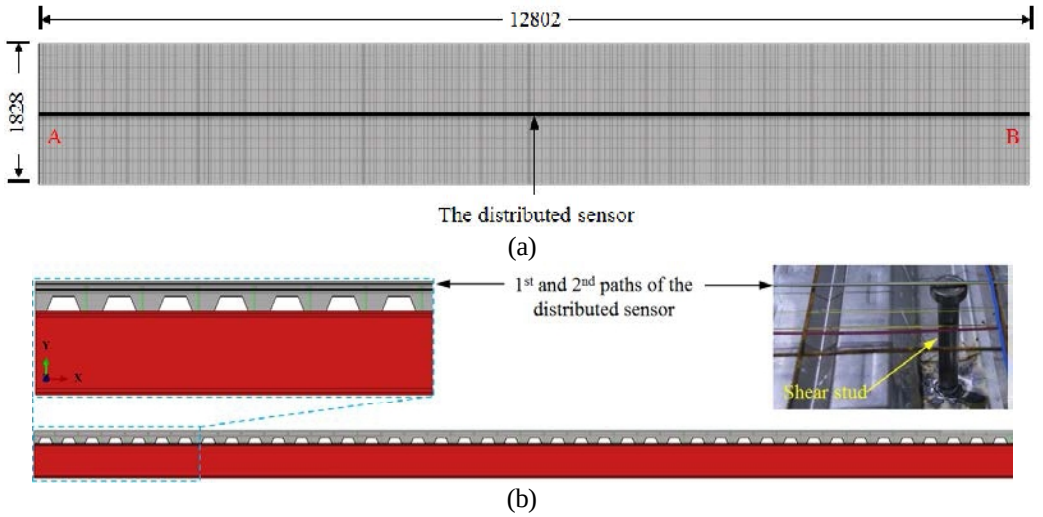

Figure 3. Layout of fiber optic sensors (unit: mm): (a) top view; (b) side view.

RESULTS AND DISCUSSIONS

Figures 4(a)–4(d) show the measurement results from the distributed fiber optic sensors embedded in the concrete topping. Figure 4(a) plots the measurement results of the Brillouin frequency distributions along the length of the distributed sensors before and after concrete placement. The Brillouin frequency increased in all the three paths. Taking the Brillouin frequency at the time of concrete placement as baseline, the Brillouin frequency shift can be determined, as plotted in Figure 4(b). The Brillouin frequency shift of the 1st path was caused only by temperature changes in the concrete topping, because the distributed sensor of the 1st path was isolated from strain change via the outer sheath. Using the calibrated temperature sensitivity coefficients, the Brillouin frequency distributions are converted into temperature distributions along the slab, which are nearly uniform as shown in Figure 4(c). The positive values of Brillouin frequency shift represent temperature increase, due to exothermic hydration reactions at early age. The Brillouin frequency shifts of the 2nd path were the combination results of both temperature increases and strain changes. After temperature compensation using the Brillouin frequency shift of the 1st path, the strain distributions along the specimen are achieved, as shown in Figure 4(d). Overall, the strain distributions along the 2nd path follow similar trends. In comparison with the temperature distributions, the strain distributions are significantly non-uniform. The strain decreases over time.

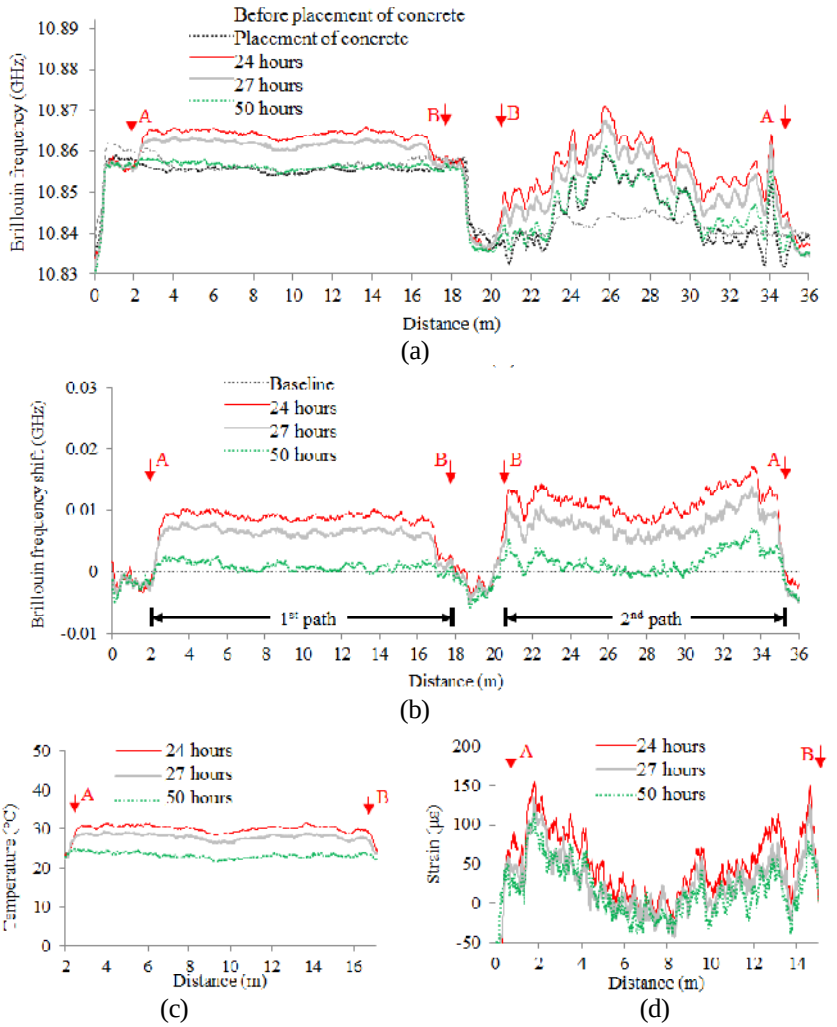

Figure 4. Measurement results from distributed sensors along the concrete: (a) Brillouin frequency distributions; (b) Brillouin frequency shifts; (c) temperature distribution; (d) strain distribution.

CONCLUSIONS

In this study, a single-mode optical fiber is used as distributed fiber optic sensor with PPP-BOTDA technology. The early-age behavior of concrete is evaluated using a long-span steel-concrete composite beam constructed in NFRL. Based on the measurement results, the following conclusions can be drawn:

(1) A practical method developed in a previous study to fabricate steel-concrete composite beam instrumented with distributed fiber optic sensors is implemented and proven to be successful. None of the installed fiber optic sensors was damaged during the placement of concrete.

(2) Temperature and strain distributions in the concrete topping are measured in the first 2 days of curing. Temperature increases due to hydration of cement, and is relatively uniform along the specimen. Non-uniform strain distributions are measured, which is possibly due to cracks in concrete. Further studies are needed to understand the effects of composite action between the shear studs and the concrete on the early-age behaviors.

ACKNOWLEDGEMENT

This work was funded by National Institute of Standards and Technology (NIST) under Award No. 70NANB13H183. The composite specimens presented in this paper were designed and constructed under NIST's Scientific and Technical Research and Services (STRS) project of Measurement of Structural Performance in Fire. The contents of this paper reflect the views of the authors, and do not necessarily reflect the official views or policies of NIST. Certain commercial equipment, instruments, or materials are identified in this paper to specify the experimental procedure. Such identification is not intended to imply recommendation by NIST, nor to imply the materials or equipment are necessarily the best available for the purpose.

REFERENCES

1. Wyrzykowski, M., Lura, P. (2013). Moisture dependence of thermal expansion in cement-based materials at early ages. Cement and Concrete Research, 53, 25-35.
2. Meng, W., Khayat, K.H. (2016). "Development of stay-in-pace formwork using GFRP reinforced UHPC elements", Proc. 1st Int. Interactive Symposium on UHPC, Des Moines, Iowa, USA.
3. Meng, W., Khayat, K.H. (2016). "Flexural performance of ultra-high performance concrete ballastless track slab", Proc. 2016 Joint Rail Conference, Columbia, South Carolina, USA.
4. Meng, W., Khayat, K.H. (2016). "Mechanical properties of ultra-high-performance concrete enhanced with graphite nanoplatelets and carbon nanofibers", Composites Part B: Engineering, 107, 113–122.
5. Meng, W., Lunkad, P., Kumar, A., Khayat, K.H. (2016). "Influence of silica fume and PCE dispersant on hydration mechanisms of cement." Journal of Physical Chemistry C, 120(47), 26814–26823.
6. Meng, W., Khayat, K.H. (2017). "Improving flexural behavior of ultra-high performance concrete by rheology control", Composites Part B: Engineering, 117, 26–34.
7. Hoehler, M. S., Smith, C. M., Hutchinson, T. C., Wang, X., Meacham, B. J., Kamath, P. (2017). Behavior of steel-sheathed shear walls subjected to seismic and fire loads. Fire Safety Journal.
8. Chen, Y., Tang, F., Bao, Y., Chen, G., Tang, Y. (2016) "Fe-C coated long period fiber grating sensors for steel corrosion monitoring," Optics Letters, 41(13), 344–346.
9. Tang, F., Bao, Y., Chen, Y., Tang, Y., Chen, G. (2016). "Impact and corrosion resistances of duplex epoxy/enamel coated plates," Construction and Building Materials, 112(1), 7–18.
10. Zhang, Q., Pei, S., Cheng, Z., Bao, Y., Li, Q. (2017). "Theoretical and experimental studies on internal force transfer mechanism of perfobond rib shear connector group," ASCE Journal of Bridge Engineering, 23, 04016112.

11. Zhang, Q., Jia, D., Bao, Y., Cheng, Z., Li, Q. (2017). “Analytical study on internal force transfer of perfobond rib shear connector group using a nonlinear spring model,” ASCE Journal of Bridge Engineering.
12. Li, X., Bao, Y., Xue, N., Chen, G. (2017). “Bond strength of steel bars embedded in high-performance fiber-reinforced cementitious composite before and after exposure to elevated temperatures,” Fire Safety Journal.
13. Li, X., Wang, J., Bao, Y., Chen, G. (2017) “Cyclic behavior of damaged reinforced concrete columns repaired with environment-friendly fiber-reinforced cementitious composites,” Engineering Structures, 136, 26–35.
14. Bao, Y., Meng, W., Chen, Y., Chen, G., Khayat, K.H. (2015). “Measuring mortar shrinkage and cracking by pulse pre-pump Brillouin optical time domain analysis with a single optical fiber.” Materials Letters, 145, 344-346.
15. Bao, Y., Valipour, M., Meng, W., Khayat, K.H., Chen, G. (2017). “Distributed fiber optic sensor-enhanced detection and prediction of shrinkage-induced delamination of ultra-high-performance concrete bonded over an existing concrete substrate.” Smart Materials and Structures, https://doi.org/10.1088/1361-665X/aa71f4.
16. Wyrzykowski, M., Hu, Z., Ghourchian, S., Scrivener, K., Lura, P. (2017). “Corrugated tube protocol for autogenous shrinkage measurements: review and statistical assessment.” Materials and Structures, 50(1), 57.
17. Meng, W., Valipour, M., and Khayat, K.H. (2017). “Optimization and performance of cost-effective ultra-high performance concrete.” Materials and structures, 50(1), 29.
18. Meng, W., Khayat, K.H. (2016). “Experimental and numerical studies on flexural behavior of ultra-high-performance concrete panels reinforced with embedded glass fiber-reinforced polymer grids.” Journal of Transportation Research Record, 2592, 38–44.
19. Zhang, Q., Cheng, Z., Cui, C., Bao, Y., He, J, Li, Q. (2017). “Analytical model for frictional resistance between cable and saddle of suspension bridges equipped with vertical friction plates,” ASCE Journal of Bridge Engineering, 22(1), 04016103.
20. Al-Tarawneh, M., Huang, Y. (2016). “Glass fiber-reinforced polymer packaged fiber Bragg grating sensors for low speed weight-in-motion measurements.” Optical Engineering, 55(8), 086107.
21. Huang, Y., Zhou, Z., Zhang, Y., et al. (2010). “A temperature self-compensated LPFG sensor for large strain measurements at high temperature.” IEEE Trans. Instr. Meas., 59(11), 2997–3004.
22. Deng, F., Huang, Y., Azarmi, F., Wang, Y.C. (2017) “Pitted corrosion detection of thermal sprayed metallic coatings using fiber Bragg grating sensors”, Coatings, 7(35), 1–17.
23. Du, Y., Jothibasu, S., Zhuang, Y., Zhu, C., Huang, J. (2017). “Rayleigh backscattering based macrobending single mode fiber for distributed refractive index sensing.” Sensors and Actuators B: Chemical, 248, 346–350.
24. Bao, Y., Chen, G. (2015). “Fully-distributed fiber optic sensor for strain measurement at high temperature.” Proceedings of the 10th International Workshop on Structural Health Monitoring 2015, Stanford, California, USA.
25. Bao, Y., Chen, G. (2016). “Temperature-dependent strain and temperature sensitivities of fused silica single mode fiber sensors with pulse pre-pump Brillouin optical time domain analysis.” Measurement Science and Technology, 27(6), 65101–65111.
26. Bao, Y., Chen, G. (2016). “High temperature measurement with Brillouin optical time domain analysis.” Optics Letters, 41(14), 3177–3180.
27. Bao, Y., Chen, Y., Hoehler, S.M., Smith, M.C., Bundy, M., Chen, G. (2016). “Experimental analysis of steel beams subjected to fire enhanced by Brillouin scattering-based fiber optic sensor data,” ASCE Journal of Structural Engineering, 143(1), 04016143.
28. Bao, Y., Chen, G. (2016). “Strain distribution and crack detection in thin unbonded concrete pavement overlays with fully distributed fiber optic sensors.” Optical Engineering, 55(1), 011008.
29. Bao, Y., Tang, F., Chen, Y., Meng, W., Huang, Y, Chen, G. (2016). “Concrete pavement monitoring with PPP-BOTDA distributed strain and crack sensors,” Smart Struct & Sys, 18(3), 19p.
30. Bundy, M., Hamins, A., Gross, J., Grosshandler, W., Choe, L. (2016). “Structural fire experimental capabilities at the NIST National Fire Research Laboratory,” Fire Technology, 52(4), 959–966.
31. Heng, J., Zheng, K., Gou, C., Zhang, Y., Bao, Y. (2017). “Fatigue performance of rib-to-deck joints in orthotropic steel decks with thickened edge U-ribs,” ASCE Journal of Bridge Engineering.
32. NIST. “ Measurement of Structural Performance in Fire - Composite Floor Systems Project” https://www.nist.gov/programs-projects/measurement-structural-performance-fire-composite-floor-systems-project